Catalytic ammonia decomposition for hydrogen production on Ni, Ru and Ni-Ru supported on CeO_2

Ilaria Lucentini, Albert Casanovas, Jordi Llorca*

Institute of Energy Technologies, Department of Chemical Engineering and Barcelona Research Center in Multiscale Science and Engineering. Universitat Politècnica de Catalunya, EEBE, Eduard Maristany 10-14, 08019 Barcelona, Spain.

*Corresponding author:

Prof. Jordi Llorca

Universitat Politècnica de Catalunya

Eduard Maristany 10-14

08019 Barcelona, Spain

+34 934011708

jordi.llorca@upc.edu

ABSTRACT

Ceria-supported Ni, Ru and Ni-Ru catalysts have been tested in the catalytic decomposition of ammonia to yield hydrogen and their performance in long-term tests has been compared to alumina-supported Ni and Ru samples. The catalysts have been characterized by XRD, TPR, NH_3-TPD, HAADF-STEM, SEM, BET and XPS. Ceria-based samples are more active in ammonia decomposition with respect to their alumina-based counterparts, which has been ascribed to a particular metal-support interaction, while acidity does not seem to play an important role. Ru-based catalysts are more active than Ni-based samples, but they deactivate rapidly, in particular the Ru/Al_2O_3 sample. This is ascribed to loss of exposed Ru, as demonstrated by XPS and HAADF-STEM. Considering the high cost and limited availability of Ru, the Ni/CeO_2 catalyst appears as a promising system for ammonia decomposition due to its good performance and low cost. *In situ* XPS experiments reveal that the active sites for the catalytic decomposition of ammonia are metallic Ni and Ru. Bimetallic Ni-Ru catalysts do not outperform their monometallic counterparts, irrespective of the order in which the metals are added.

Keywords: ammonia decomposition, ceria-based catalysts, nickel catalysts, *in situ* XPS.

1. Introduction

Hydrogen is known to be a clean and environmentally sustainable energy vector. Its use in Proton Exchange Membrane Fuel Cells (PEMFC) to generate energy is a suitable alternative to the use of fossil fuels which have a high carbon footprint, as water is the only secondary product generated in the process [1-3]. One of the current challenges facing hydrogen technologies is its storage and transport [4-6]. Although hydrogen has a very

high energy density on a mass basis (119.7 MJ kg^{-1} of lower heating value at 25ºC and 1 bar, while gasoline has 44.79 MJ kg^{-1}) [7], it has a very low energy density on a volume basis due to its low molecular weight (8.96 GJ m^{-3}, while gasoline has 31.17 GJ m^{-3}, both referred to as liquid fuels) [8], which leads to storage difficulties. In addition, hydrogen tends to diffuse through the material which is used to contain and transport it, resulting in embrittlement of the storage material [9-10].

The most common method of hydrogen storage nowadays is as a compressed gas at pressures of up to 700 bar at room temperature [11]. Alternatively, liquid hydrogen of higher volumetric energy density can be used; however, liquid hydrogen is cryogenic and boils at -252.9°C at 1 bar [12-13]. There is an intermediate method, cryo-compression, in which hydrogen is stored in the form of gas cooled until the pressure required for its compression reduces to 350 bar [14]. All these techniques require a large amount of energy [15]. Another method is the adsorption of hydrogen on a material with high surface area and porosity, such as metal hydrides and organic frameworks (MOFs), because they have well known and controllable structural characteristics [16]. However, in this case the adsorption of hydrogen still has a low volumetric density, energy is irremediable lost in transporting the carrier [17] and there are difficulties in their regeneration processes [18]. A completely different approach to store hydrogen is chemical storage in the form of another compound that contains hydrogen, this allows for transportation with relative ease [19-22]. Hydrogen is then generated on site through a chemical reaction (decomposition, steam reforming, oxidative reforming, etc.) [23-26].

Ammonia has been frequently considered as a feasible option for chemical storage because of its high hydrogen content (17.8% by weight and a volumetric density of 121 kg H_2 m^{-3} at 10 bar) and absence of carbon. It has an energy density in volume of 13.6 GJ m^{-3}, a value that fall between hydrogen and gasoline [27-30]. If the ammonia used in the

process is produced through renewable resources, the entire hydrogen production process has a very low carbon footprint. Ammonia liquefies at low pressure, 8.6 bar at 20°C, so its transport and storage is relatively easy [31]. With regard to safety issues, ammonia has a narrow combustion range, 16-25% in air, compared to that of 4-75% for hydrogen, and a concentration as low as 5 ppm can be detected easily by smell [32].

In order to use ammonia as an energy carrier, the development of catalytic systems able to yield hydrogen at efficient rates is needed. The decomposition reaction of ammonia is endothermic (equation 1):

$$2\ NH_{3(g)} \leftrightarrows N_{2(g)} + 3\ H_{2(g)} \qquad \Delta H°=46.22\ kJ\ mol^{-1} \qquad \text{(eq. 1)}$$

High operating temperatures are required to bring the ammonia decomposition reaction to completion and so to produce hydrogen very high in purity. This is necessary when the decomposition is used to provide H_2 to a PEMFC because it deteriorates irreversibly at low concentrations of ammonia (ca. 0.1 ppm) [28]. The high temperature of the decomposition reaction leads to the necessity for a supply of energy and, for that reason, appropriate catalysts are being developed to run the reaction at a lower temperature with high efficiency. Furthermore, a hydrogen selective metallic membrane can be used to remove hydrogen from the reactor and shift the reaction equilibrium [33].

A considerable number of studies have appeared in recent literature regarding ammonia as a decomposition catalyst. There is a general agreement that ruthenium is the most active metal for this reaction [34–39]. Ganley *et al.* have studied a number of metals supported on Al_2O_3 pellets and they have reported that the activity follows the order: Ru > Ni > Rh > Co > Ir > Fe > Pt > Cr > Pd > Cu [40]. Although nickel is less active than Ru, it is interesting due to its low cost compared to ruthenium [41]. Using high throughput techniques, Liu *et al.* have tested a high number of transition metals supported on SiO_2, proving that the most active metals at 843 K are Ru > Ni > Co > Ir > Ag, while the other

transition metals present very low catalytic activity [42]. To enhance the catalytic activity of some of the low-cost metals different bimetallic compositions have been explored because it is known that bimetallic systems usually have superior properties with respect to their monometallic counterparts [43]. Cobalt has been combined with Mo [44] and Fe [45,46]. Iron has been combined with Mo [47]. Nickel has been studied in the bimetallic systems Ni-Ir [48], Ni-Pt [49], Ni-Mo [50,51], Ni-Pd [52] and Ni-Fe [53]. All these bimetallic catalysts have shown better ammonia decomposition performances than their monometallic counterparts, but still ammonia conversion is low at temperatures below 550ºC [37]. Regarding the supports, Al_2O_3, SiO_2, MgO and both structured and non-structured carbon have been widely used [34,35,37]. Cerium dioxide has rarely been used as a catalyst support in this reaction but, in addition to providing reactive surfaces, ceria prevents metal sintering at high temperatures through robust metal-support interactions [54,55]. Regarding the use of ceria in catalytic ammonia decomposition, it has been employed as a support for Ni catalysts by Muroyama *et al.* [56] and Deng *et al.* [57] with contradictory results, and as a dopant by Liu *et al.* [58], Yao *et al.* [59] and Zhao *et al*. [60] who have studied its promoting effect in Ni supported on silica and Co-Mo supported on carbon nanotubes. Nickel supported on ceria-zirconia and cobalt supported on MgO-CeO_2 have also been tested [57,61]. However, less attention has been payed to the architecture of the active sites provided by these catalysts and, to the best of our knowledge, no dedicated *in situ* and/or *operando* studies have been attempted. Obviously, the characterization of the active sites would provide valuable information when preparing a new generation of highly-active catalysts for ammonia decomposition to yield hydrogen. With that purpose, here we have performed an *in situ* X-ray photoelectron spectroscopy (XPS) study of CeO_2-supported Ni and Ru catalysts under ammonia decomposition conditions to get an insight into the nature of the active sites. The performance of Ni, Ru and bimetallic Ni-Ru on alumina and ceria supports are also compared.

2. Materials and methods

2.1 Catalyst preparation

Nanopolycrystalline CeO_2 was prepared using an ultrasonic atomizer (*Sonozap HTWS30)* and a hydrothermal reactor (*Reactor Chemipress-500*) by following the procedure described in [62]. A solution of 6.07 g of $Ce(NO_3)_3.6H_2O$ (*Alfa Aesar*) in 35 ml of distilled water was atomized over an agitated solution of 2.00 g of NaOH (*Fisher Scientific*) in 245 ml of distilled water at 400-500 rpm. After that, the resulting solution was agitated for 30 minutes at room temperature. This precursor solution was then treated in the hydrothermal reactor at 150°C for 24 hours in order to produce the polycrystalline cerium oxide. The resulting material was centrifuged (15 min at 10,000 rpm), sonicated, and cleaned with distilled water (three times) and ethanol (twice) until a neutral pH was obtained. The material was dried at 70°C overnight, ground into an agate mortar and calcined at 450°C for 4 hours (2°C min^{-1}). Alumina was prepared by calcination of γ-$Al(OH)_3$ (*Panreac Química S.A.U.*) at 500°C for 5 hours (10°C min^{-1}).

The CeO_2 and Al_2O_3 supports were impregnated using the incipient wetness (IWI) method from aqueous solutions of $Ni(CH_3COO)_2{\cdot}4H_2O$ (*Probus*) and/or $RuCl_3$ (*Tokyo Chemical Industries*). The amount of nickel in the catalysts was fixed at 10% w/w, while ruthenium content was 2% w/w. After impregnation, catalysts were dried at 100°C for 24 h and calcined at 450ºC (Ni catalysts) and 400°C (Ru catalysts) for 4 h (5°C min^{-1}). Bimetallic catalysts were prepared on CeO_2 by three different methods: (1) IWI of the previously prepared ceria supported nickel catalyst with $RuCl_3$ dissolved in water, (2) IWI of the previously prepared ceria supported ruthenium catalyst with $Ni(CH_3COO)_2{\cdot}4H_2O$ dissolved in water, and (3) co-impregnation of $RuCl_3$ and $Ni(CH_3COO)_2{\cdot}4H_2O$ on CeO_2. Catalysts were calcined at 450°C for 4 h (5°C min^{-1}). They were labeled as (1) Ru-Ni, (2) Ni-Ru and (3) NiRu, respectively.

2.2 Catalyst characterization

Powder X-ray Diffraction (XRD) patterns were recorded using a Siemens D5000 diffractometer using Cu Kα radiation (45 kV, 35 mA) in Bragg-Brentano geometry. The diffraction patterns were recorded in steps of 0.02° at 1 second per step. The Debye-Sherrer equation was used to measure crystallite size. Temperature Programmed Reduction (TPR) experiments were performed with a Chemstar-TPX instrument equipped with a Thermal Conductivity Detector (TCD). Samples (50 mg) were first heated from RT to 450°C in argon flow (50 ml min^{-1}, 10°C min^{-1}), kept at 450°C for 10 minutes and cooled down to 50ºC under Ar flow. TPR was then performed from 50ºC up to 500ºC (10°C min^{-1}) under 10% H_2 in Ar (the total flow was 50 ml min^{-1}) and kept at 500ºC for 30 minutes. Temperature Programmed Desorption of Ammonia (NH_3-TPD) analysis was carried out to determine catalyst acidity with a BELCAT-M instrument equipped with TCD. Samples (50 mg) were first heated from RT to 450°C in Ar flow (35 ml min^{-1}, 10°C min^{-1}), kept at 450°C for 20 minutes and cooled down to 50°C under Ar. Samples were then exposed to pulse titration by using a loop of a known volume of ammonia in Ar flow until saturation. NH_3-TPD was finally performed from 50°C up to 800°C with a heating rate of 10°C min^{-1} under Ar (35 ml min^{-1}) and kept at 800°C for 30 minutes. Nitrogen adsorption isotherms were performed at 77 K using a Micromeritics ASAP2020 gas adsorption instrument. The materials were degassed at 500ºC for 10 h prior to the adsorption experiments. The specific surface areas were calculated using the Brunauer–Emmett–Teller (BET) method. Scanning Electron Microscopy (SEM) images were recorded at 5 kV using a Zeiss Neon40 Crossbeam Station instrument equipped with a field emission source. The catalyst was suspended in ethanol, and a drop of the solution was placed on a silicon wafer. Scanning transmission electron microscopy under high-angle annular dark field mode (HAADF-STEM) was carried out with a FEI TECNAI F20 S/TEM instrument equipped with a field

emission electron source operated at 200 kV. Samples were prepared by dispersing the catalysts in methanol; a drop of the suspension was then allowed to evaporate on a holey carbon coated copper grid. Surface chemical characterization was done by X-ray Photoelectron Spectroscopy (XPS) on a SPECS system equipped with a XR50 source operating at 150 W and a Phoibos 150 MCD-9 detector. The pass energy of the hemispherical analyzer was set at 25 eV and the energy step of high-resolution spectra was set at 0.1 eV. The pressure in the analysis chamber was always below 10^{-7} Pa, and binding energy (BE) values were referred to the C 1s peak at 284.8 eV. Data processing was performed with the CasaXPS software. Atomic fractions were calculated using peak areas normalized on the basis of acquisition parameters after background subtraction, experimental sensitivity factors and transmission factors provided by the manufacturer. Cerium 3d spectra were deconvoluted using six peaks for Ce^{4+} (V, V'', V''', U, U'' and U'''), corresponding to three pairs of spin-orbit doublets and four peaks for Ce^{3+} (V_0, V', U_0 and U'), which correspond to two doublets, based on the peak positions reported by Mullins et al. [63], where U and V refer to the $3d_{3/2}$ and $3d_{5/2}$ spin-orbit components, respectively. Aluminum 2p spectra were deconvoluted using two peaks for Al^{3+} (Al $2p_{3/2}$ and Al $2p_{1/2}$) using the work of Rotole et al. as a reference [64]. Nickel 2p deconvolution was based on a comparison of the reported peak positions and FWHM by Davidson et al. [65], Roy et al. [66], Mansour et al. [67] and Biesinger et al. [68]. Nickel 2p spectra were deconvoluted using four peaks and four satellites for Ni^{2+} corresponding to four pairs of spin-orbit doublets, two peaks and two satellites for Ni^{3+} corresponding to two pairs of spin-orbit doublets and two peaks and two satellites for Ni^{0} corresponding to two pairs of spin-orbit doublets. Ruthenium 3d spectra were deconvoluted following the works of Morgan [69], Bianchi et al. [70] and Elmasides et al. [71]. For the deconvolution of Ru spectra four peaks for Ru^{4+} and two peaks for Ru^{0} have been used, corresponding to four and two pairs of spin-orbit doublets, respectively. *In situ* ammonia decomposition experiments were

performed in a reaction chamber connected to the XPS analysis chamber that allowed for dynamic treatments up to 600°C under atmospheric pressure. The temperature of the sample was measured with a thermocouple in contact with the sample holder, which was heated with an IR lamp. The reactants were introduced by means of mass flow controllers ($Ar:NH_3$=4:1, molar basis, total 25 ml min^{-1}) and the evolution of products was followed by a mass spectrometer Dycor LC-D Series Residual Gas Analyzer (1-100 amu). For the experiments, samples were heated under the reaction mixture of Ar and NH_3. At the end of each experiment (30 min), the sample was cooled down to ambient temperature before transferring it to the analysis chamber. The sequence of spectra recorded and experiments performed were (i) sample as prepared, (ii) activation under H_2 at 300°C, (iii) ammonia decomposition at 350°C, (iv) ammonia decomposition at 450°C, (v) ammonia decomposition at 550°C, (iv) reduction under H_2 at 550°C.

2.3 Catalytic tests

The catalytic reactions were carried out at atmospheric pressure in a 316-grade stainless steel tubular reactor with a diameter of ¼" OD and a wall thickness of 0.035". The mass of powdered catalyst used was 100 mg, which was diluted with SiC to obtain a fixed bed volume of 0.45 cm^3. The reactor was placed inside a vertical furnace connected to an external thermal control system to regulate the temperature of the reactor within ±0.1°C. The reactor effluent was analyzed on-line with a mass spectrometer (OmniStar GSD320 O2 series). In this study, an instrumental error of ±5% in the mass spectrometer results is considered. The catalytic activity was measured between 350 and 600ºC at steps of 50ºC (30 min at each temperature). Catalysts were activated at 300ºC for 1 h with H_2 (10% in Ar, 80 ml min^{-1}, 10ºC min^{-1}). Reaction tests were conducted using a total gas flow of 23 ml min^{-1} and a $Ar:NH_3$ ratio of 1.3:1 (molar basis), which corresponds to a gas hourly space

velocity (GHSV) of 3,067 h^{-1}. Stability tests were conducted for 100 h at 450°C. Ammonia conversion, $NH_{3\ conv}$, is defined as (equation 2):

$$NH_{3\ conv.} = \frac{Q\ NH_{3\ initial} - Q\ NH_{3\ final}}{Q\ NH_{3\ initial}} * 100 \qquad \text{(eq. 2)}$$

3. Results and discussion

3.1 Catalytic ammonia decomposition

Figure1 shows variable-temperature ammonia conversion of the catalysts prepared in this study as well as the bare CeO_2 and Al_2O_3 supports and a blank run of the reactor employed. As expected, in all cases ammonia decomposition increased with reaction temperature and the only products obtained were H_2 and N_2 in a H_2:N_2 ratio of 3:1. Also, the activity of the ceria and alumina supports was negligible taking into account the ammonia conversion levels obtained in the blank run. For each support, Ru-based catalysts were more active than their Ni-based counterparts. In particular, Ru/CeO_2 showed high ammonia conversion at low temperatures with respect to Ni/CeO_2, 98 vs. 63% at 450ºC. On the other hand, for each metal, CeO_2-supported catalysts were much more active than their respective Al_2O_3-supported counterparts. Concerning the three Ni-Ru/CeO_2 bimetallic samples, their activity was almost the same at each temperature (± 4% of difference) and it was intermediate between those exhibited by Ru/CeO_2 and Ni/CeO_2, irrespective of the order in which the metals are added. Overall, the ammonia decomposition activity followed the trend: Ru/CeO_2 > Ru-Ni/CeO_2 ~ Ni-Ru/CeO_2 ~ $NiRu/CeO_2$ > Ru/Al_2O_3 > Ni/CeO_2 >> Ni/Al_2O_3. The superior performance of Ru-based catalysts with respect to Ni-based ones in the decomposition of ammonia to produce hydrogen has already been described in the literature [40]. In this work we demonstrate that CeO_2 is a better support than the conventional Al_2O_3 used for this reaction and that

the bimetallic system Ni-Ru/CeO_2 does not allow for further improvement of the results already obtained with Ru/CeO_2. In order to compare the catalytic performances obtained in this work with those reported in literature, the turnover frequency values (TOF) have been calculated. Yin et al. [72] reported a TOF_{H_2} of 1.1 s^{-1} (150,000 ml h^{-1} g_{cat}^{-1}) for Ru supported on CNTs at 400ºC, while Wang et al. [73] and Yin et al. [74] reported TOF_{H_2} values of 4.8 s^{-1} (60,000 ml h^{-1} g_{cat}^{-1}) and 3 s^{-1} (30,000 ml h^{-1} g_{cat}^{-1}) at the same temperature after promoting Ru/CNTs with K. The TOF_{H_2} obtained in this study for Ru/CeO_2 at 400ºC (13,800 ml h^{-1} g_{cat}^{-1}) is 1.8 s^{-1}, which is in the range of the TOF values reported for the most active Ru/CNTs catalysts. The TOF_{H_2} of Ru/Al_2O_3 under the same conditions is 1.0 s^{-1}, also in the range of the values reported in the literature for alumina-supported Ru catalysts ([74,75]). Considering Ni catalysts, Ni/Al_2O_3 exhibits a TOF_{H_2} value of 0.01 s^{-1} and Ni/CeO_2 of 0.03 s^{-1} at 400ºC; these values are lower than that reported by Choudhary et al. using Ni/SiO_2, 0.4 s^{-1} at 400ºC (30,000 ml h^{-1} g_{cat}^{-1}) [75].

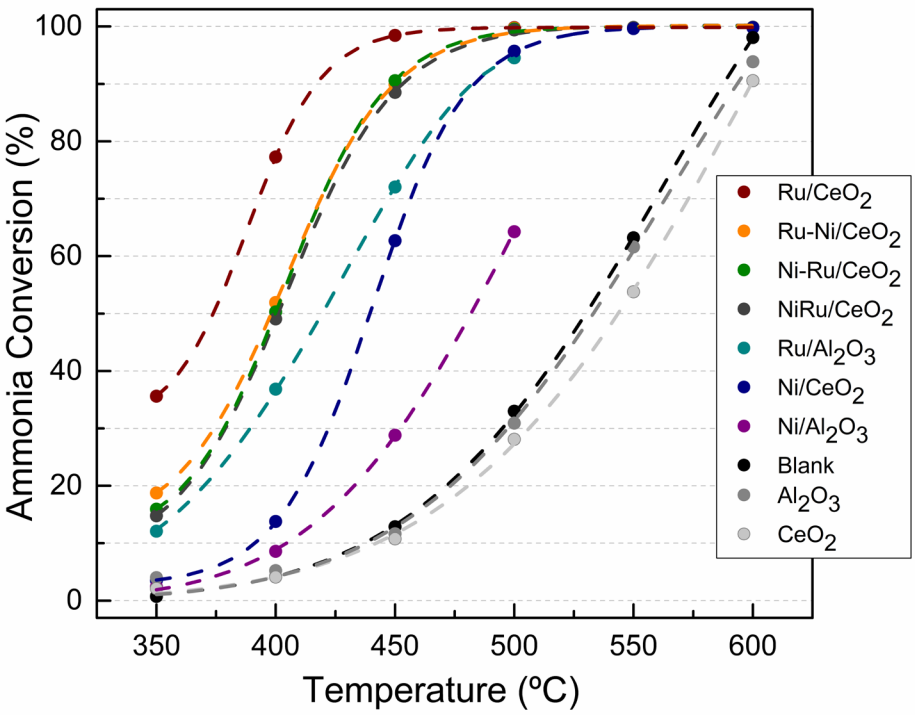

Figure 1. Variable-temperature ammonia conversion. Reaction test conditions: GHSV of 3,067 h^{-1}, 0.1 g of catalyst, F/W of 13.8 L h^{-1} g^{-1}, Ar:NH_3=1.3:1, 1 atm.

An interesting point to discuss is the different dynamics exhibited by the Ru/CeO_2 and Ni/CeO_2 catalysts during the reaction tests. Figure 2 shows the catalytic performance over time at each temperature tested. According to the results outlined above, the Ni/CeO_2 sample is poorly active at low temperatures (up to 400ºC), but it is important to note that at these low temperatures it deactivates significantly. However, at 450ºC there is a progressive activation of the catalysts over time on stream and the conversion of ammonia increases sharply. At temperatures of 500ºC and higher the conversion of ammonia progressively increases and the catalyst shows stable ammonia conversion. In contrast, the Ru/CeO_2 catalyst shows a distinct behavior. The sample only shows a slight deactivation at the lowest temperature tested, 350ºC, and at temperatures of 400ºC and above the catalyst shows a readily stable ammonia conversion. This issue is related to the formation of active sites in the catalysts and will be studied in detail by *in situ* XPS in section 3.3.

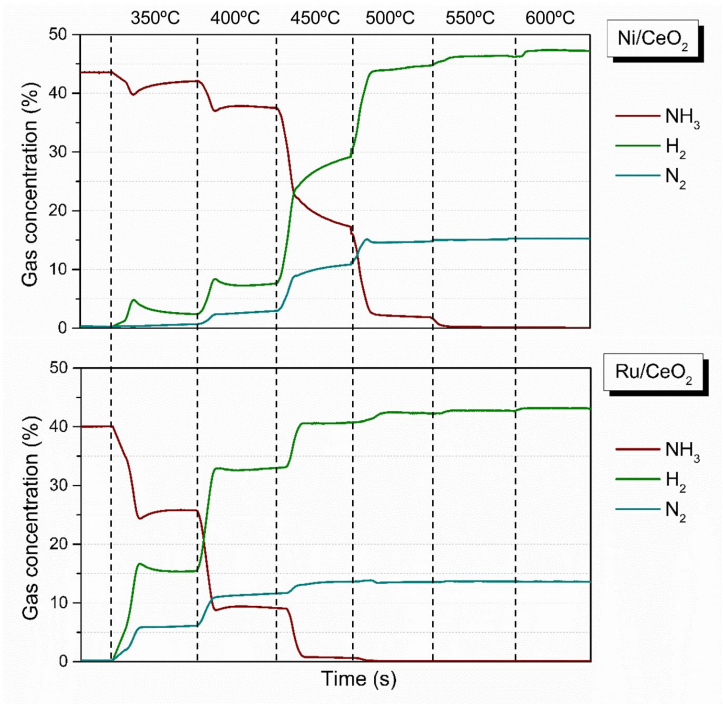

Figure 2. Variable-time gas concentration measured over Ni/CeO_2 and Ru/CeO_2. Reaction test conditions: GHSV of 3,067 h^{-1}, 0.1 g of catalyst, F/W of 13.8 L h^{-1} g^{-1}, Ar:NH_3=1.3:1, 1 atm.

3.2 Characterization

The two oxides used as catalytic supports were analyzed before the deposition of the metals by SEM to study their morphology and BET for the surface area. Figure 3 shows representative SEM images of Al_2O_3 (a and b) and CeO_2 (c and d). Alumina particles have a hexagonal, platelet-like morphology with a basal plane size ranging from about 50 to 500 nm. Ceria particles are much smaller, have a rounded morphology and measure from 5 to 10 nm. According to the results of the BET analysis, the surface area of ceria is 70.3 $m^2 g^{-1}$ and that of alumina is 231 $m^2 g^{-1}$.

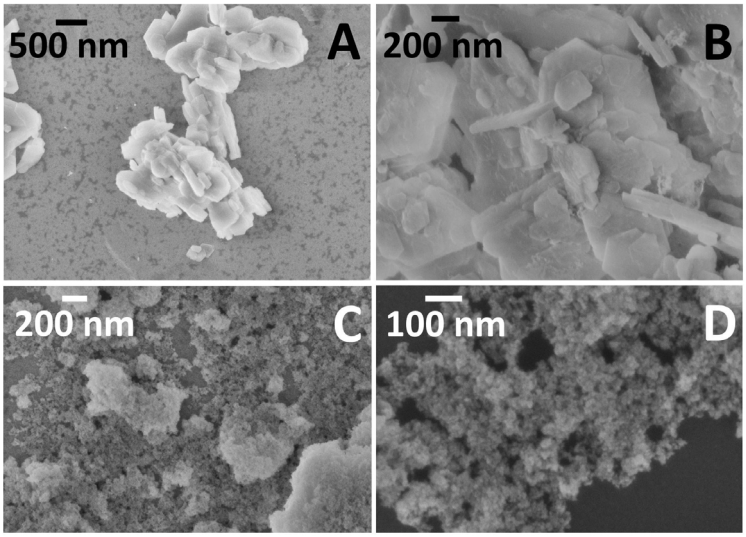

Figure 3. SEM images of Al_2O_3 (a,b) and CeO_2 (c,d) at different magnifications.

In Figure 4, HAADF-STEM images of Ru and Ni supported on ceria and alumina are presented along with the particle size histograms of the metal nanoparticles. The hexagonal, platelet-like morphology of the Al_2O_3 support is nicely seen in the low-magnification image in Figure 4. Alumina platelets measure 50-400 nm along their basal plane, in accordance to SEM results, and show a thickness of about 20 nm (see arrow in Figure 4, Ru/Al_2O_3, low magnification). At high magnification the high porosity of the

alumina support at the nanometer level is also observed, which accounts for the high BET surface area measured. Ruthenium particles of about 8 nm in diameter are very well distributed over the alumina support in Ru/Al_2O_3 (Figure 4, Ru/Al_2O_3, red circles). Nickel particles of about 3.3 nm in diameter are also highly dispersed over the alumina support in Ni/Al_2O_3 (Figure 4, Ni/Al_2O_3, green circles). Ru/CeO_2 contains ceria nanoparticles with a round-shape morphology of about 4-10 nm in size, in accordance with SEM observations (Figures 3 and 4) and Ru particles of about 7 nm (Figure 4, Ru/CeO_2, red circles). In Ni/CeO_2, Ni particles exhibit a diameter of about 5 nm (Figure 4, Ni/CeO_2, green circles). In both cases, random energy-dispersive X-ray analyses reveal the metals are highly dispersed over the ceria support.

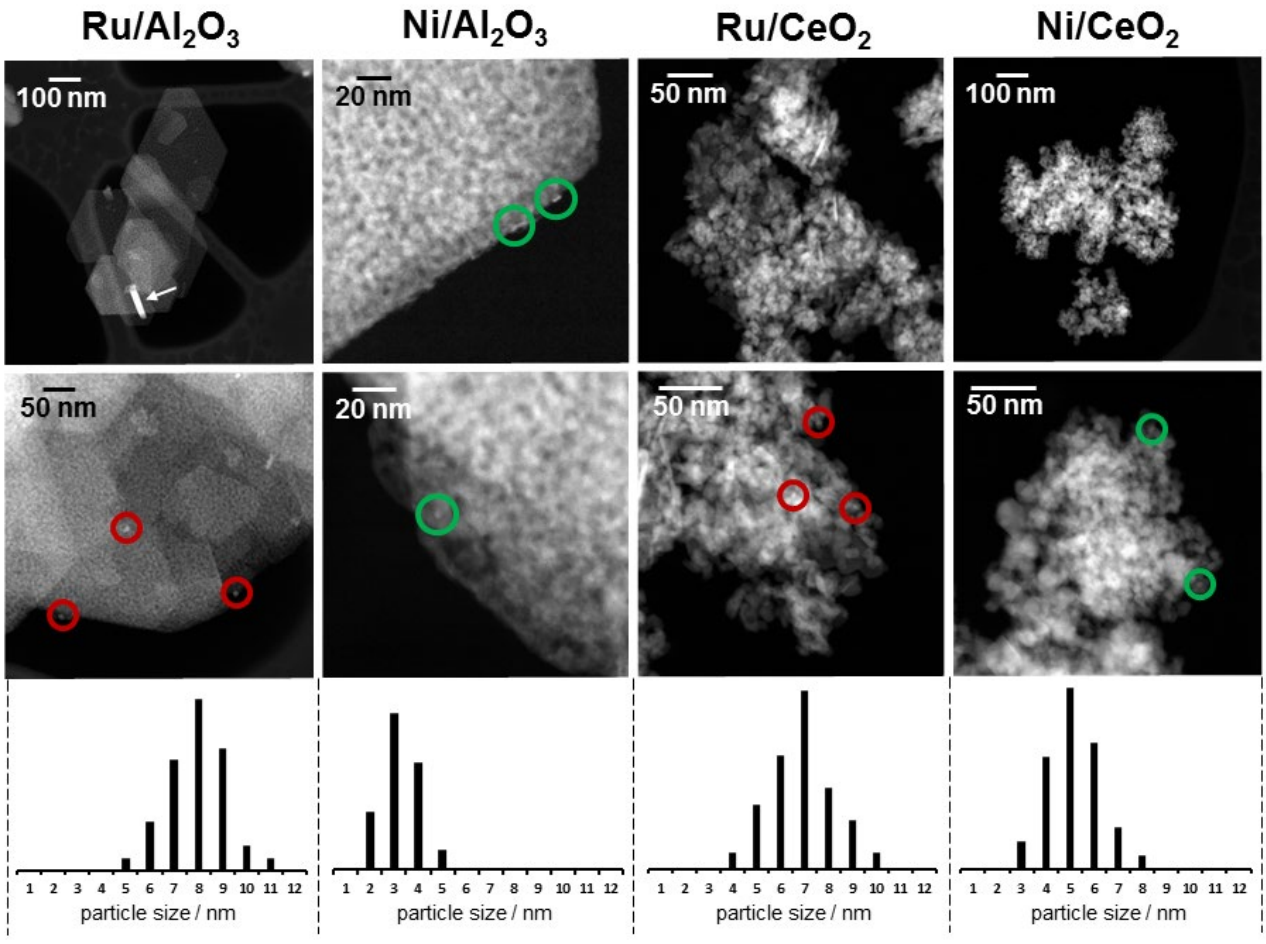

Figure 4. HAADF-STEM images and particle size histograms of Ru and Ni particles.

Figure 5 shows the H_2-TPR profiles of the ceria-based catalysts. As reported elsewhere [76,77], reduction of CeO_2 occurs at temperatures between 300 and 600°C. The hydrogen consumption by CeO_2 starting at about 300ºC is assigned to the reduction of surface Ce(IV) to Ce(III). Incorporation of Ni and Ru facilitates the reduction of ceria at the surface, which takes place at about 370°C in Ni/CeO_2 and 320°C in Ru/CeO_2, in accordance to a different metal-support interaction and hydrogen spillover ability [77-81]. At lower temperatures there is the reduction of nickel oxide at about 215°C and ruthenium oxide at ca. 90°C, which is in accordance with literature values [82,83]. The bimetallic samples exhibit reduction peaks at lower temperatures, 80 and 180°C. This is in accordance with the data reported by Wang et al. [84] showing that ruthenium can facilitate the reduction of NiO and CeO_2 due to hydrogen spillover.

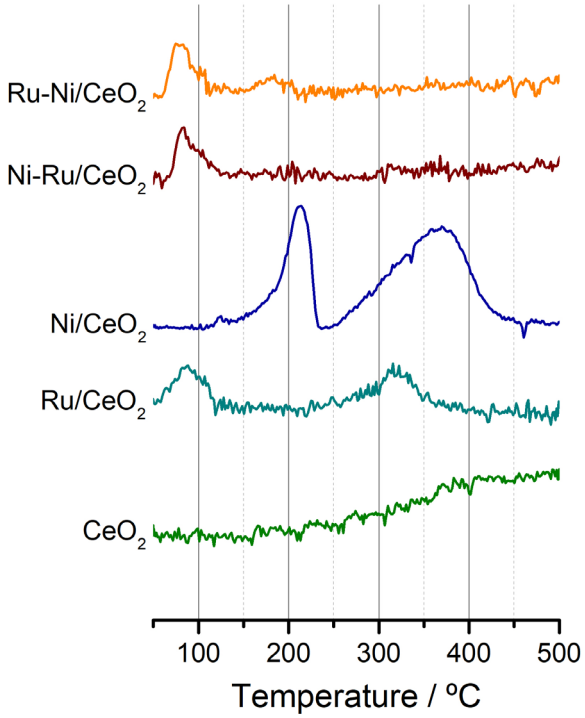

Figure 5. Temperature programmed reduction profiles of ceria-based catalysts.

Figure 6 shows the XRD patterns of the catalysts as prepared and after reduction with H_2 at 300°C (the activation temperature). As expected, the XRD profiles of the ceria-supported samples are dominated by the characteristic peaks of the CeO_2 phase, with a mean crystallite size of about 10 nm as deduced from the Scherrer equation, in accordance with SEM and STEM results. Additional peaks of RuO_2 are observed in the Ru/CeO_2 catalyst as prepared; their very low intensity indicates a very high dispersion. After reduction, the RuO_2 peaks in Ru/CeO_2 disappear and no peaks of metallic Ru are seen, again pointing to an excellent metal dispersion, in accordance with TEM results. The XRD profile of the Ni/CeO_2 sample as prepared shows peaks corresponding to NiO. These peaks disappear after the reduction treatment and new peaks appear corresponding to the appearance of Ni metal, in accordance with the TPR profile discussed above (Figure 5). Figure 6 also contains the XRD profiles of the alumina-supported catalysts. The alumina support shows a pattern corresponding to χ-Al_2O_3, which is in accordance with the thermodynamically stable alumina phase predicted through the thermal sequence of the aluminum hydroxides [85] according to the alumina precursor (γ-$Al(OH)_3$ or gibbsite) and the calcination temperature (500°C). In addition to the alumina peaks, samples Ru/Al_2O_3 and Ni/Al_2O_3 as prepared exhibit the characteristic peaks of RuO_2 and NiO, respectively.

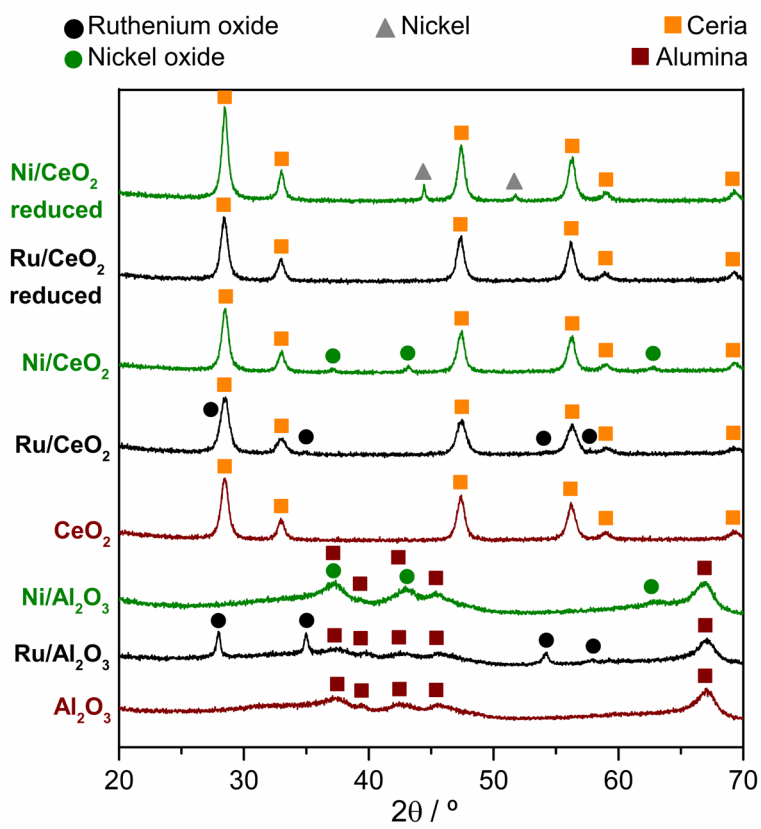

Figure 6. XRD patterns of the samples as prepared and after standard activation (reduction in H_2 at 300ºC for 1 h).

Alumina-based catalysts have been used thoroughly for the decomposition of ammonia given the robustness and acid character of Al_2O_3 [86]. In this work, we have shown that Ni/CeO_2 and Ru/CeO_2 catalysts perform much better than Ni/Al_2O_3 and Ru/Al_2O_3, respectively. Thus, acidity alone does not seem to be the main driving force for this reaction. We have performed NH_3 pulse titration to obtain the total acidity values of the different catalysts as well as NH_3-TPD to study the strength of the acid sites (Figure 7). As expected, the total acidity of the alumina-based samples is considerably higher than that of the ceria-based catalysts, 0.4-0.6 vs. 0.1-0.2 $mmol_{NH3}$ g^{-1}, respectively. On the other hand, alumina-based samples exhibit a larger amount of strong acid sites (sites that desorb NH_3 at high temperature) than ceria-based catalysts. The addition of metals in all cases results in an enhancement of weak-medium acid sites and in the partial disappearance of the

strong acid sites. From these results it is possible to conclude that acidity does not play a main role in the catalytic decomposition of ammonia. The high catalytic performance of the ceria-based catalysts in the decomposition of ammonia may be related to the well-known redox characteristics of ceria and/or to a specific metal-support interaction between ceria and the metals. To get more insight into the behavior of these catalysts, an *in situ* study by X-ray photoelectron spectroscopy has been carried out over Ni/CeO_2 and Ru/CeO_2.

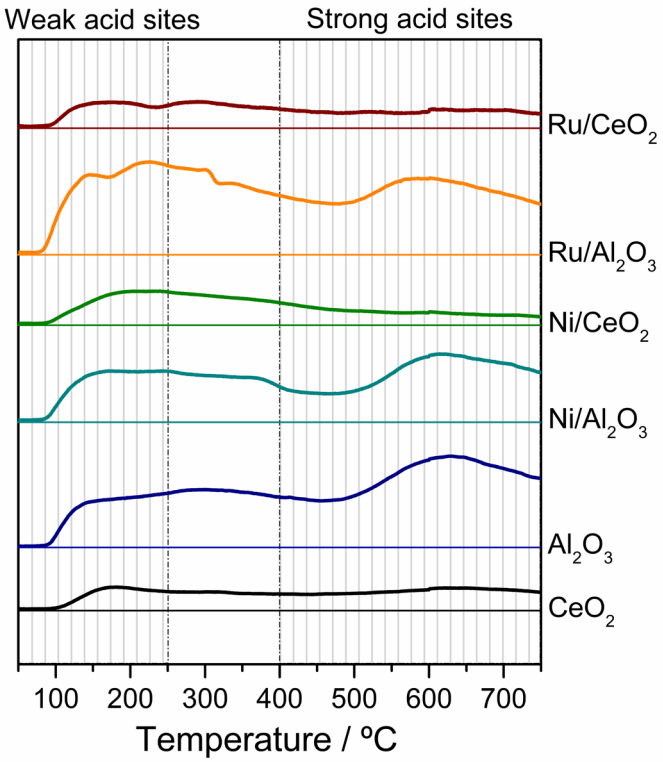

Figure 7. NH_3-TPD over different catalysts. Weak and strong acid site ranges are shown as patterned area.

3.3 In situ XPS

To precisely identify the active metal species present in the Ni/CeO_2 and Ru/CeO_2 catalysts an *in situ* study was performed by X-ray photoelectron spectroscopy. XP spectra were recorded over each sample after calcination, after reduction at 300ºC (activation treatment), after ammonia decomposition reaction at 350, 450 and 550ºC, and after

reduction at 550ºC. Figure 8 shows the Ce 3d and Ni 2p signals recorded after each experiment over Ni/CeO_2, Figure 11 corresponds to the Ce 3d and Ru 3d signals recorded over Ru/CeO_2 after exactly the same treatments and Table 1 compiles the binding energy values and surface atomic ratios recorded for each sample under different conditions.

The fresh Ni/CeO_2 catalyst exhibits Ni $2p_{3/2}$ bands at 854-856 eV and an intense satellite signal at 862 eV. The $2p_{1/2}$ bands overlap partially with those of Ce 3d (Figure 8). These binding energy values and the presence of the strong satellite both indicate the presence of oxidized Ni species, which is in accordance with the XRD results discussed above (Figure 6). After activation, the intensity of the satellite signals decrease and new signals appear at 853 and 870 eV in the Ni $2p_{3/2}$ and Ni $2p_{1/2}$ spectra, respectively, which is characteristic of metallic Ni. This is in accordance with the TPR profile recorded for this sample (Figure 5) and XRD (Figure 6). At the same time, the atomic ratio Ni/Ce decreases from 1.1 (fresh sample) to 0.63 (Table 1), indicating that Ni sintering occurs upon reduction. The sintering of Ni is also observed clearly in the XRD profiles shown in Figure 6 from the FWHM values of NiO (fresh catalyst) and metallic Ni (after reduction). However, after the sample is exposed to ammonia at 350ºC, these bands disappear, indicating oxidation of Ni metal into Ni oxide and, simultaneously, the Ni/Ce atomic ratio increases from about 0.63 to 1.0 (Table 1) due to Ni redispersion upon oxidation. This fact explains the low activity of the catalyst at this reaction temperature (Figure 9) and the deactivation observed in Figure 2. When the ammonia decomposition was conducted at 450ºC the activity of the catalyst increased sharply (Figure 9) and it progressively activated to yield hydrogen (Figure 2). The XP spectrum recorded after ammonia decomposition at this temperature shows again the bands at 853 and 870 eV characteristic of Ni metal, the satellite signal becomes less intense, and the Ni/Ce atomic value decreases again to ca. 0.5. Therefore, it is safe to conclude that the active species for ammonia decomposition is metallic Ni. Accordingly, at 550ºC, where the catalyst was fully active and stable (Figure

2), the amount of Ni metal increases with respect to oxidized species from about 31 to 44% (Table 1) and the TOF_{H2} reaches its maximum value (Figure 9). The persistence of oxidized Ni at the catalyst surface is ascribed to oxygen donation from the ceria support [54]. Regarding the Ce 3d spectra, the amount of Ce(III) is maintained approximately constant at 30% (Table 1), independent of the reaction conditions. However, it is interesting to note that at 550ºC the amount of Ce(III) is significantly larger under pure H_2 compared to ammonia decomposition conditions (61 vs. 42%), but the amount of Ni metal is similar under the ammonia decomposition conditions with respect to pure H_2 (48 vs. 44%). This constitutes additional evidence that hydrogen is likely produced during ammonia decomposition on Ni particles or at the interface between Ni metal nanoparticles and the CeO_2 support, where it has a stronger reduction effect. Finally, it is worth mentioning that there is a correlation between the extent of ammonia decomposition and hydroxyl bands on the surface of the catalyst. Figure 10 shows the O 1s region of the activated sample and after the ammonia decomposition reaction at 350, 450 and 550ºC. In the spectra, the most intense signal at 528.9 eV corresponds to lattice oxygen, and that at about 531.5 eV corresponds to surface hydroxyl groups. The intensity of the hydroxyl band is low in the sample after activation and after reaction at 350ºC, when the catalyst is poorly active for ammonia decomposition. In contrast, at 450 and 550ºC the hydroxyl band increases progressively as does the catalytic activity (Figure 2). This result is aligned with DFT calculations reported for the decomposition of ammonia on Ir(100), which shows that surface oxygen and hydroxyl species promote NH_3 dehydrogenation steps [87].

Table 1. Surface atomic ratios and binding energies of Ni/CeO_2 and Ru/CeO_2 from *in situ* analysis.

				Ni $2p_{3/2}$ Binding Energy (eV)	
Ni/CeO_2	Ni/Ce	Ce(III)/Ce (%)	Ni^0/Ni (%)	Ni^{ox}	Ni^0
as prepared	1.1	30	0	854.1, 855.8 , 856.0	-
activated at 300ºC	0.63	29	33	854.6, 856.0	852.9
reaction 350ºC	1.0	17	0	853.9, 855.3, 856.2	-
reaction 450ºC	0.54	24	31	854.7, 856.0	853.0
reaction 550ºC	0.53	42	44	854.2, 856.0	852.7
reduced at 550ºC	0.46	61	48	853.9, 856.0	852.8
				Ru $3d_{5/2}$ Binding Energy (eV)	
Ru/CeO_2	Ru/Ce	Ce(III)/Ce (%)	Ru^0/Ru (%)	Ru^{ox}	Ru^0
as prepared	0.38	23	0	281.5, 283.7	-
activated at 300ºC	0.48	46	18	280.8, 283.2	280.3
reaction 350ºC	0.17	32	16	280.7	279.9
reaction 450ºC	0.18	31	27	280.8	280.0
reaction 550ºC	0.18	44	38	280.7	280.1
reduced at 550ºC	0.20	45	60	281.0	280.4

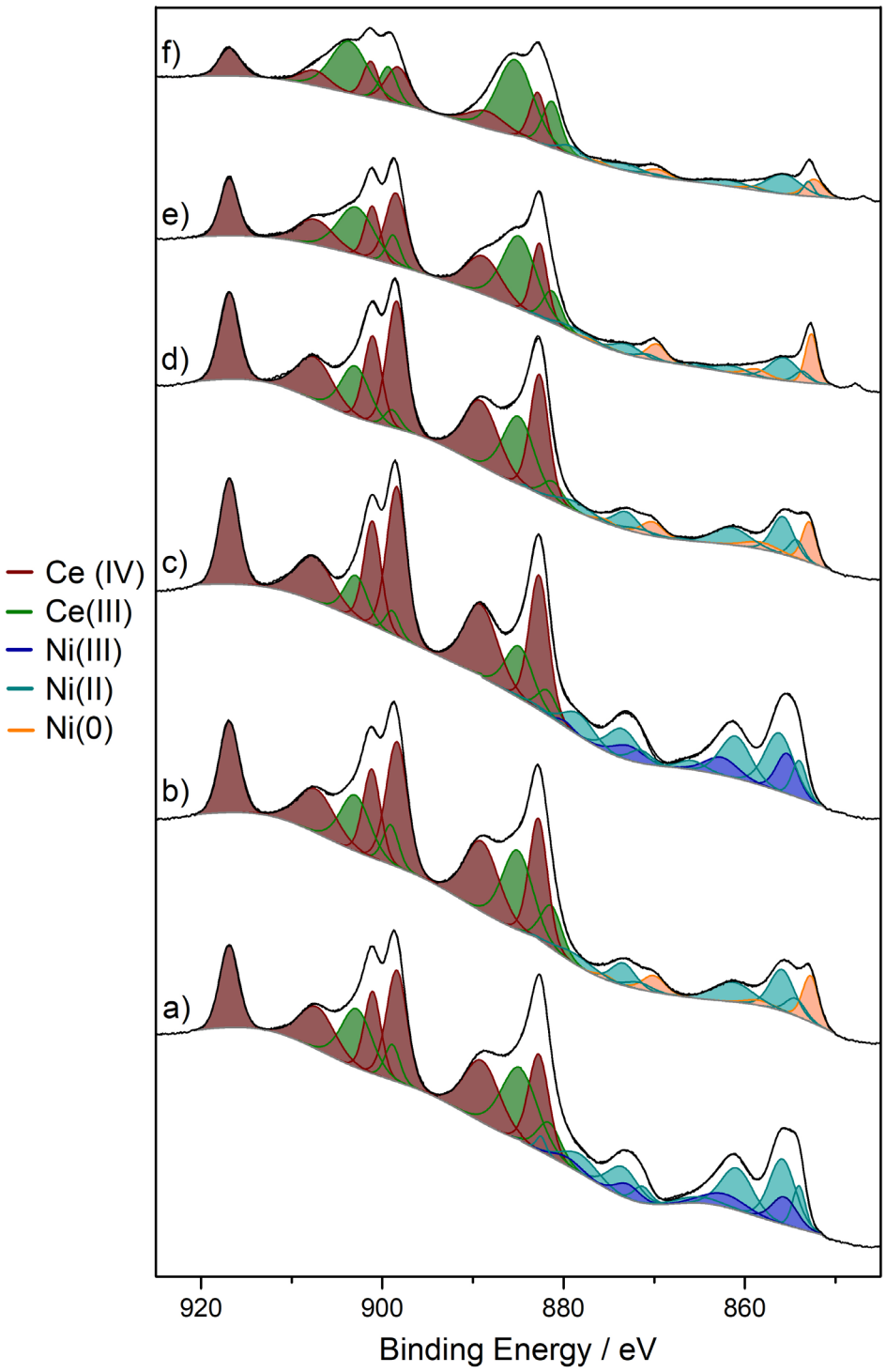

Figure 1. Ce 3d and Ni 2p spectra of *in situ* XPS experiments carried out over Ni/CeO_2 a) as prepared, b) after activation with H_2 at 300ºC, c) after ammonia decomposition at 350ºC, d) 450ºC, e) 550ºC, and f) after reduction at 550ºC.

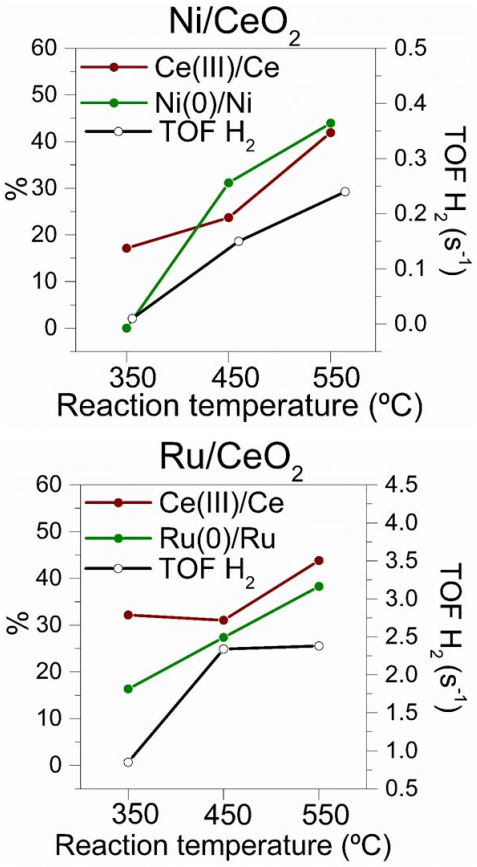

Figure 9. Atomic ratios from *in situ* XPS analysis and TOF_{H2} of Ni/CeO_2 and Ru/CeO_2.

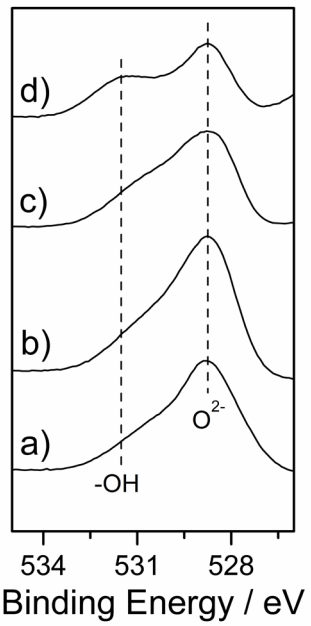

Figure 10. O1s spectra of *in situ* XPS carried out on Ni/CeO_2 catalyst a) after activation with H_2 at 300ºC, b) after ammonia decomposition at 350ºC, c) 450ºC, and d) 550ºC.

The analysis of the *in situ* XPS experiment recorded over the Ru/CeO_2 catalyst reveals some interesting differences (Figure 11). Initially, the fresh sample only exhibits Ru $3d_{5/2}$ bands at about 281.5-283.7 eV (Table 1) that partially overlap with the C 1s signal. This value corresponds to Ru oxide species, in accordance to XRD results (Figure 6). When the sample is activated (reduced at 300ºC) a new band at 280.3 eV (Table 1) appears, which is characteristic of Ru metal. After ammonia decomposition at 350ºC, ca. 16% of Ru persists in a metallic state (Table 1). At this temperature the catalyst already showed stable ammonia conversion of 36% (Figure 2). At higher reaction temperatures (450 and 550ºC), the catalyst achieved its maximum activity (Figure 9) and the spectra recorded show the presence of Ru metal (Figure 11). This again points to the fact that the metal function is required and that Ru metal is involved in the active site for ammonia decomposition. On the other hand, the amount of Ce(III) during the reaction is higher in Ru/CeO_2 compared to Ni/CeO_2 (Figure 9). In Ru/CeO_2 the amount of Ce(III) is 32-44% (compared to 17-42% in Ni/CeO_2) (Table 1). This is a direct consequence of the presence of Ru metal, which facilitates hydrogen spillover and the associated reduction of Ce(IV) into Ce(III). Finally, it has been observed that the atomic Ru/Ce ratio has remarkably decreased during the experiments, from 0.48 in the reduced sample to 0.20 at the end of the study. Under the same conditions with Ni/CeO_2 the atomic Ni/Ce ratio decreased only from 0.6 to 0.5 (Table 1). This suggests that stability issues may be important during ammonia decomposition, particularly over Ru catalysts.

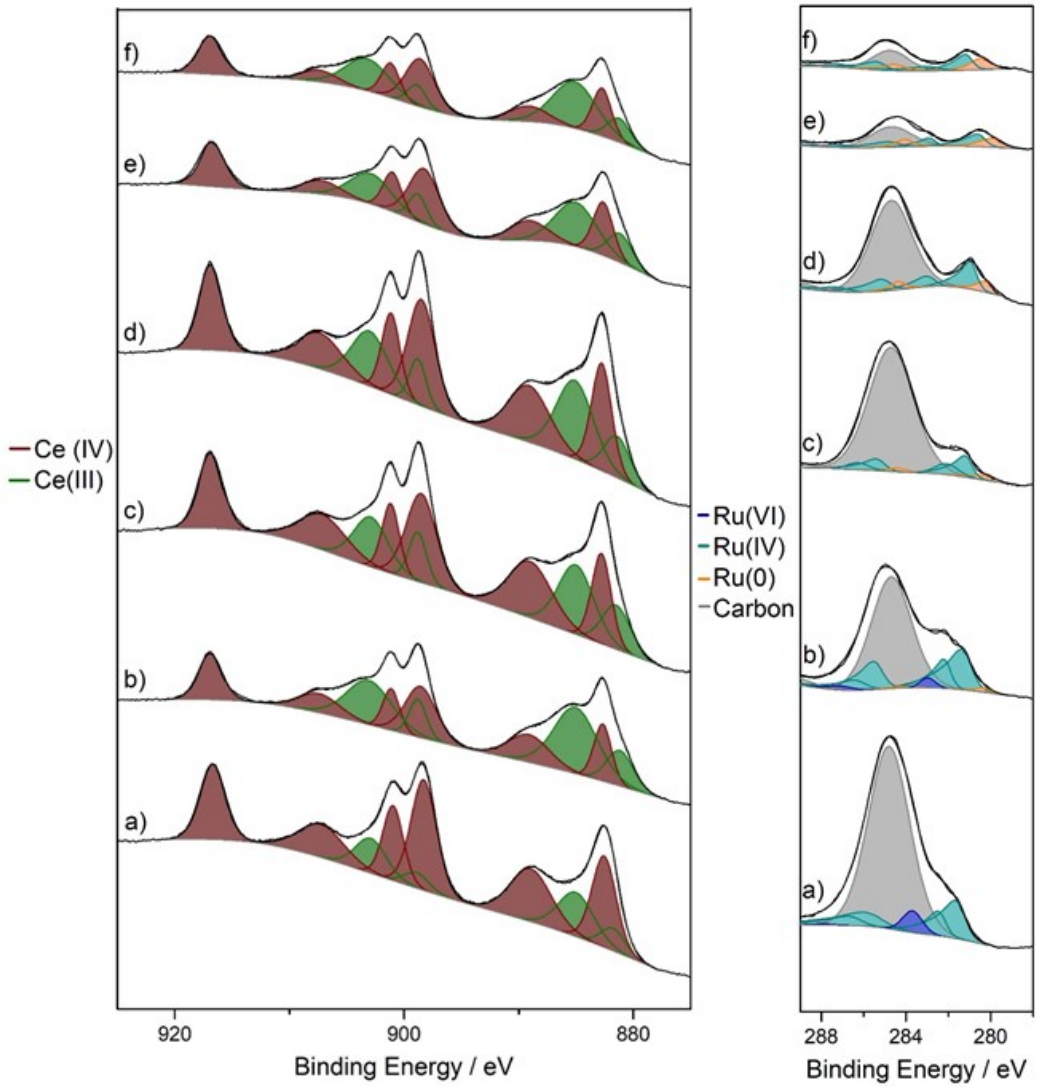

Figure 11. Ce 3d and Ru 3d spectra of *in situ* XPS experiments carried out over Ru/CeO_2 a) as prepared, b) after activation with H_2 at 300ºC, c) after ammonia decomposition at 350ºC, d) 450ºC, e) 550ºC, and f) after reduction at 550ºC.

3.4 Stability test

Long term (100 h) stability tests were conducted over Ru/CeO_2, Ni/CeO_2, Ru/Al_2O_3 and Ni/Al_2O_3 at 450ºC to study the robustness of the catalysts (Figure 12). The high stability of the Ni-based catalysts in terms of ammonia conversion after 100 h is remarkable; in fact the Ni/Al_2O_3 catalyst activated progressively over time on stream and the Ni/CeO_2 catalyst

remained unaltered. In contrast, the Ru-based samples deactivated under the same reaction conditions. In particular, the Ru/Al_2O_3 sample deactivated drastically and after 85 h on stream its performance was surpassed by Ni/CeO_2. Interestingly, the use of ceria as a catalyst support greatly increases the stability of Ru compared to Ru/Al_2O_3. The Ru/CeO_2 catalyst is also deactivated, but to a lesser extent.

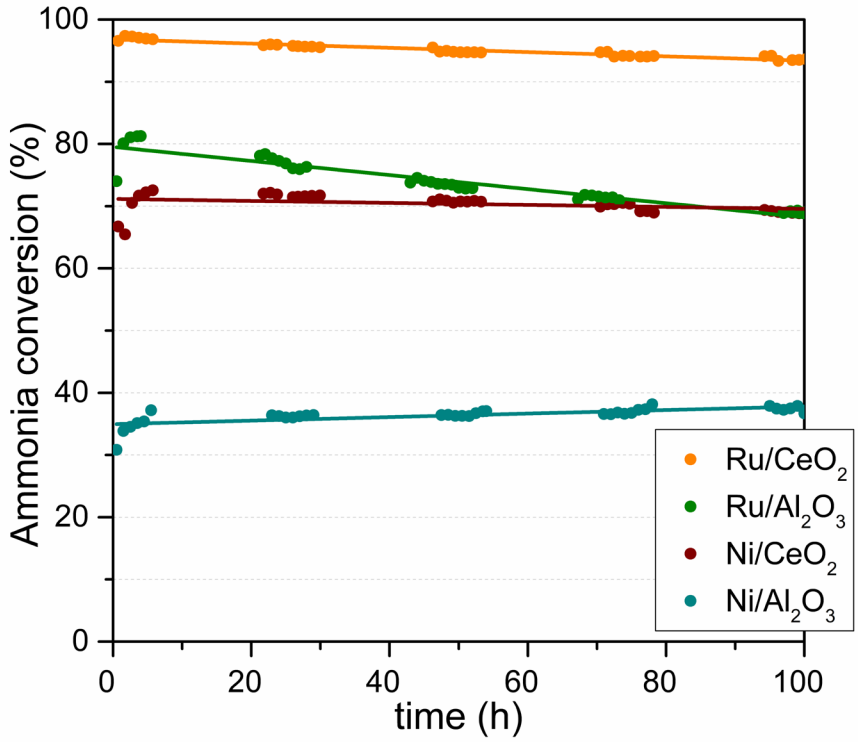

Figure 12. Stability test of Ru and Ni supported on ceria and alumina. GHSV of 3,067 h^{-1}, 0.1 g of catalyst, F/W of 13.8 L $h^{-1}g^{-1}$, Ar:NH_3=1.3:1, 450ºC and 1 atm.

The *in situ* XPS study discussed in section 3.3 over Ru/CeO_2 revealed clearly that the Ru/Ce ratio decreased over time (from Ru/Ce 0.48 to 0.20, Table 1), suggesting that deactivation is likely caused by the progressive decrease of exposed Ru. To further confirm this, at the end of the stability tests the samples were analyzed by XPS (Figure 13), and the Ru/Ce ratio in Ru/CeO_2 was only 0.05. Thus, we safely conclude that

deactivation is due to a severe loss of exposed Ru. As expected, at the end of the stability test both Ni^0 and Ru^0 species are clearly identified, in accordance with the *in situ* XPS study reported above.

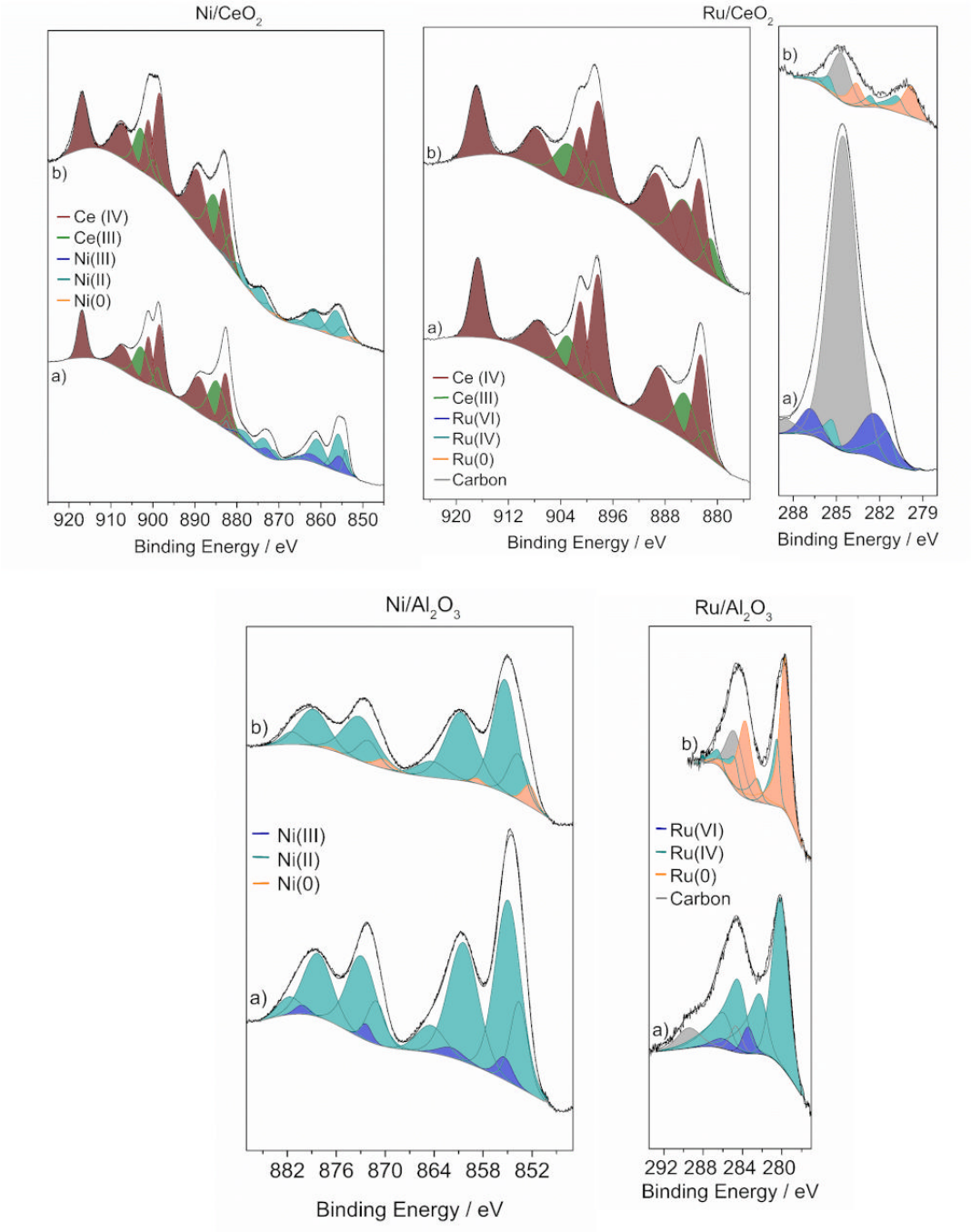

Figure 13. Ce 3d, Ni 2p and Ru 3d XP spectra recorded before (a) and after stability tests (b).

Finally, the catalysts were also studied by HAADF-STEM at the end of the stability test (Figure 14). The particle size of Ru in the post-reacted Ru/Al_2O_3 catalyst was about 40 nm, which is much larger than the Ru particle size in the fresh sample (ca. 8 nm, Figure 4). Thus, sintering of Ru accounts for the progressive and strong deactivation of Ru/Al_2O_3 (Figure 12). In contrast, the particle size of Ru in the post-reacted Ru/CeO_2 catalyst was about 6 nm, which is slightly lower than the Ru particle size in the fresh sample (7 nm, Figure 4). Therefore, taking into account the decrease in particle size as determined by HAADF-STEM and the decrease of the Ru/Ce surface atomic ratio as determined by XPS, the deactivation of Ru/CeO_2 is ascribed to a progressive volatilization of Ru. According to this, the Ni particle size in the Ni/Al_2O_3 sample after the stability test was about 7 nm (Figure 14), which is larger than that of the fresh sample (3.3 nm, Figure 4), whereas the Ni particle size in the Ni/CeO_2 catalyst was preserved at about 5 nm after the stability test.

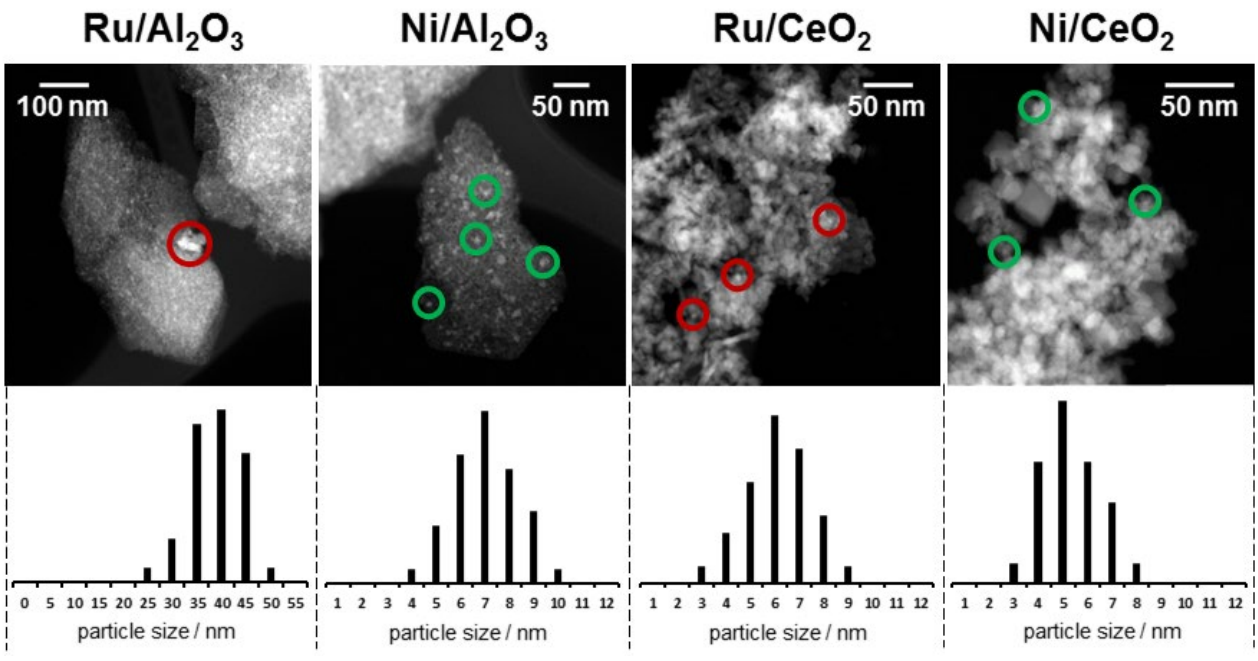

Figure 14. HAADF-STEM images and particle size histograms of Ru and Ni particles after the stability test.

In summary, Ru-based catalysts, although they exhibit a high initial activity for ammonia decomposition, undergo deactivation. Taking into account that Ni-based samples are stable under the same operation conditions and that Ni/CeO_2 is much more active in ammonia decomposition than Ni/Al_2O_3, catalyst Ni/CeO_2 it is thus considered an appropriate choice for producing hydrogen from ammonia decomposition in practical applications.

4. Conclusions

A series of Ni, Ru and Ni-Ru supported on Al_2O_3 and CeO_2 have been prepared, characterized and tested in the decomposition of ammonia to obtain hydrogen. The initial activity of the ammonia decomposition follows the trend: Ru/CeO_2 > $Ru\text{-}Ni/CeO_2$ ~ $Ni\text{-}Ru/CeO_2$ ~ $NiRu/CeO_2$ > Ru/Al_2O_3 > Ni/CeO_2 >> Ni/Al_2O_3. The catalysts as prepared contain a good dispersion of NiO and RuO_2 over the supports, which evolve into metal nanoparticles after an activation treatment under H_2 at 300°C. Ru-based catalysts are more active than Ni-based, but deactivate either by metal sintering (Ru/Al_2O_3) or by Ru volatilization (Ru/CeO_2). For Ni-based catalysts, at low ammonia decomposition temperatures (up to 450°C) the Ni metal nanoparticles reoxidize and deactivate, whereas at temperatures above 450°C they are maintained in their reduced state and the catalysts become very active and stable. In this work we have demonstrated that CeO_2 is a better support than conventional Al_2O_3 for this reaction and that the bimetallic system $Ni\text{-}Ru/CeO_2$ does not allow for further improvement of the results obtained over Ru/CeO_2. In terms of cost and catalytic stability, the Ni/CeO_2 catalyst is preferred.

Acknowledgments

This work has been funded by projects MINECO/FEDER ENE2015-63969-R and GC 2017 SGR 128. JL is a Serra Húnter Fellow and is grateful to ICREA Academia program. IL is grateful to MINECO for the BES-2016-076507 grant. We are also grateful to M. Romanini and M. Domínguez for their technical assistance.

Competing interests statement

The authors have no competing interests to declare.

References

[1] Cheng X, Shi Z, Glass N, Zhang L, Zhang J, Song D, et al. A review of PEM hydrogen fuel cell contamination: Impacts, mechanisms, and mitigation. J Power Sources 2007;165:739–56. doi:10.1016/j.jpowsour.2006.12.012.

[2] Grigoriev SA, Porembsky VI, Fateev VN. Pure hydrogen production by PEM electrolysis for hydrogen energy. Int J Hydrogen Energy 2006;31:171–5. doi:10.1016/j.ijhydene.2005.04.038.

[3] Barbir F, Gómez T. Efficiency and economics of proton exchange membrane (PEM) fuel cells. Int J Hydrog Energy 1997;22:1027–37.

[4] Crabtree GW, Dresselhaus MS, Buchanan MV. The Hydrogen Economy. Phys Today 2004;57:39–45. doi:10.1063/1.1878333.

[5] Rowsell JLC, Yaghi OM. Strategies for hydrogen storage in metal-organic frameworks. Angew Chem. Int. Ed. 2005;44:4670–9. doi:10.1002/anie.200462786.

[6] Nijkamp MG, Raaymakers JEMJ, van Dillen AJ, de Jong KP. Hydrogen storage using physisorption – materials demands. Appl Phys A 2001;72:619–23.

doi:10.1007/s003390100847.

[7] White CM, Steeper RR, Lutz AE. The hydrogen-fueled internal combustion engine: a technical review. Int J Hydrogen Energy 2006;31:1292–305. doi:10.1016/j.ijhydene.2005.12.001.

[8] van den Berg AWC, Areán CO. Materials for hydrogen storage: current research trends and perspectives. Chem Commun 2008:668–81. doi:10.1039/B712576N.

[9] Robertson IM, Sofronis P, Nagao A, Martin ML, Wang S, Gross DW, et al. Hydrogen Embrittlement Understood. Metall Mater Trans A Phys Metall Mater Sci 2015;46A:2323–41. doi:10.1007/s11661-015-2836-1.

[10] Irani R. Hydrogen Storage: High-Pressure Gas Containment. MRS Bulletin 2002;27(9):680–2. doi:10.1557/mrs2002.221.

[11] Zheng J, Liu X, Xu P, Liu P, Zhao Y, Yang J. Development of high pressure gaseous hydrogen storage technologies. Int J Hydrogen Energy 2012;37:1048–57. doi:10.1016/j.ijhydene.2011.02.125.

[12] Mori D, Hirose K. Recent challenges of hydrogen storage technologies for fuel cell vehicles. Int J Hydrogen Energy 2009;34:4569–74. doi:10.1016/j.ijhydene.2008.07.115.

[13] Züttel A. Hydrogen storage methods. Naturwissenschaften 2004;91:157–72. doi:10.1007/s00114-004-0516-x.

[14] Ahluwalia RK, Hua TQ, Peng JK, Lasher S, McKenney K, Sinha J, et al. Technical assessment of cryo-compressed hydrogen storage tank systems for automotive applications. Int J Hydrogen Energy 2010;35:4171–84. doi:10.1016/j.ijhydene.2010.02.074.

[15] Hwang HT, Varma A. Hydrogen storage for fuel cell vehicles. Curr Opin Chem Eng 2014;5:42–8. doi:10.1016/j.coche.2014.04.004.

[16] Suh MP, Park HJ, Prasad TK, Lim D-W. Hydrogen storage in metal-organic frameworks. Chem Rev 2012;112:782–835. doi:10.1021/cr200274s.

[17] Murray LJ, Dincă M, Long JR. Hydrogen storage in metal–organic frameworks. Chem Soc Rev 2009;38:1294–314. doi:10.1039/b802256a.

[18] Sakintuna B, Lamari-Darkrim F, Hirscher M. Metal hydride materials for solid hydrogen storage: A review. Int J Hydrogen Energy 2007;32:1121–40. doi:10.1016/j.ijhydene.2006.11.022.

[19] Subrahmanyam KS, Kumar P, Maitra U, Govindaraj A, Hembram KPSS, Waghmare U V., et al. Chemical storage of hydrogen in few-layer graphene. Proc Natl Acad Sci 2011;108:2674–7. doi:10.1073/pnas.1019542108.

[20] Jain IP. Hydrogen the fuel for 21st century. Int J Hydrogen Energy 2009;34:7368–78. doi:10.1016/j.ijhydene.2009.05.093.

[21] Dutta S. A review on production, storage of hydrogen and its utilization as an energy resource. J Ind Eng Chem 2014;20:1148–56. doi:10.1016/j.jiec.2013.07.037.

[22] Biniwale RB, Rayalu S, Devotta S, Ichikawa M. Chemical hydrides: A solution to high capacity hydrogen storage and supply. Int J Hydrogen Energy 2008;33:360–5. doi:10.1016/j.ijhydene.2007.07.028.

[23] Kojima Y, Suzuki KI, Fukumoto K, Sasaki M, Yamamoto T, Kawai Y, et al. Hydrogen generation using sodium borohydride solution and metal catalyst coated on metal oxide. Int J Hydrogen Energy 2002;27:1029–34. doi:10.1016/S0360-3199(02)00014-9.

[24] Dincer I. Green methods for hydrogen production. Int J Hydrogen Energy 2012;37:1954–71. doi:10.1016/j.ijhydene.2011.03.173.

[25] Eberle U, Felderhoff M, Schüth F. Chemical and physical solutions for hydrogen storage. Angew Chemie Int Ed 2009;48:6608–30. doi:10.1002/anie.200806293.

[26] Otsuka K, Kaburagi T, Yamada C, Takenaka S. Chemical storage of hydrogen by modified iron oxides. J Power Sources 2003;122:111–21. doi:10.1016/S0378-7753(03)00398-7.

[27] Jensen JO, Li Q, Bjerrum NJ. The energy efficiency of onboard hydrogen storage techniques. In: Palm J, editor. Energy Effic., InTech; 2010, p. 143–56.

[28] Makepeace JW, Wood TJ, Hunter HMA, Jones MO, David WIF. Ammonia decomposition catalysis using non-stoichiometric lithium imide. Chem Sci 2015;6:3805–15. doi:10.1039/c5sc00205b.

[29] Klerke A, Christensen CH, Nørskov JK, Vegge T. Ammonia for hydrogen storage: challenges and opportunities. J Mater Chem 2008;18:2304. doi:10.1039/b720020j.

[30] Zamfirescu C, Dincer I. Using ammonia as a sustainable fuel. J Power Sources 2008;185:459–65. doi:10.1016/j.jpowsour.2008.02.097.

[31] Lan R, Irvine JTS, Tao S. Ammonia and related chemicals as potential indirect hydrogen storage materials. Int J Hydrogen Energy 2012;37:1482–94. doi:10.1016/j.ijhydene.2011.10.004.

[32] Zamfirescu C, Dincer I. Ammonia as a green fuel and hydrogen source for vehicular applications. Fuel Process Technol 2009;90:729–37. doi:10.1016/j.fuproc.2009.02.004.

[33] Itoh N, Oshima A, Suga E, Sato T. Kinetic enhancement of ammonia decomposition

as a chemical hydrogen carrier in palladium membrane reactor. Catal Today 2014;236:70–6. doi:10.1016/j.cattod.2014.02.054.

[34] García-Bordejé E, Armenise S, Roldán L. Toward practical application of H_2 generation from ammonia decomposition guided by rational catalyst design. Catal Rev - Sci Eng 2014;56:220–37. doi:10.1080/01614940.2014.903637.

[35] Bell TE, Torrente-Murciano L. H_2 Production via Ammonia Decomposition Using Non-Noble Metal Catalysts: A Review. Top Catal 2016;59:1438–57. doi:10.1007/s11244-016-0653-4.

[36] Schüth F, Palkovits R, Schlögl R, Su DS. Ammonia as a possible element in an energy infrastructure: catalysts for ammonia decomposition. Energy Environ Sci 2012;5:6278–89. doi:10.1039/c2ee02865d.

[37] Mukherjee S, Devaguptapu S V, Sviripa A, Lund CRF, Wu G. Low-temperature ammonia decomposition catalysts for hydrogen generation. Appl Catal B Environ 2018;226:162–81. doi:10.1016/j.apcatb.2017.12.039.

[38] Yin SF, Xu BQ, Zhou XP, Au CT. A mini-review on ammonia decomposition catalysts for on-site generation of hydrogen for fuel cell applications. Appl Catal A Gen 2004;277:1–9. doi:10.1016/j.apcata.2004.09.020.

[39] Duan X, Zhou X, Chen D. Structural manipulation of the catalysts for ammonia decomposition. Catalysis 2013;25:118–40. doi:10.1039/9781849737203-00118.

[40] Ganley JC, Thomas FS, Seebauer EG, Masel RI. A *priori* catalytic activity correlations: The difficult case of hydrogen production from ammonia. Catal Letters 2004;96:117–22. doi:10.1023/B:CATL.0000030108.50691.d4.

[41] Chiuta S, Everson RC, Neomagus HWJP, van der Gryp P, Bessarabov DG. Reactor

technology options for distributed hydrogen generation via ammonia decomposition: A review. Int J Hydrogen Energy 2013;38:14968–91. doi:10.1016/j.ijhydene.2013.09.067.

[42] Liu H, Wang H, Jianghan S, Sun Y, Liu Z. Preparation and evaluation of ammonia decomposition catalysts by high-throughput technique. React.Kinet.Catal.Lett 2008;93:11–7. doi: 10.1007/s11144-008-5155-3

[43] Jiang H-L, Xu Q. Recent progress in synergistic catalysis over heterometallic nanoparticles . J Mater Chem 2011;21:13705–25. doi:10.1039/c1jm12020d.

[44] Ji J, Duan X, Qian G, Zhou X, Tong G, Yuan W. Towards an efficient CoMo/γ-Al_2O_3 catalyst using metal amine metallate as an active phase precursor: Enhanced hydrogen production by ammonia decomposition. Int J Hydrogen Energy 2014;39:12490–8. doi:10.1016/j.ijhydene.2014.06.081.

[45] Xun Y, He X, Yan H, Gao Z, Jin Z, Jia C. Fe- and Co-doped lanthanum oxides catalysts for ammonia decomposition: Structure and catalytic performances. J Rare Earths 2017;35:15–23. doi:10.1016/S1002-0721(16)60167-9.

[46] Zhang J, Mu J, Zheng W, Wang D, Su D, Schlo R. Individual Fe-Co Alloy Nanoparticles on Carbon Nanotubes: Structural and Catalytic Properties. Nano Lett 2008;8:2738-43. doi:10.1021/nl8011984.

[47] Lorenzut B, Montini T, Bevilacqua M, Fornasiero P. FeMo-based catalysts for H_2 production by NH_3 decomposition. Appl Catal B Environ 2012;125:409–17. doi:10.1016/j.apcatb.2012.06.011.

[48] Han X, Chu W, Ni P, Luo SZ, Zhang T. Promoting effects of iridium on nickel based catalyst in ammonia decomposition. J Fuel Chem Technol 2007;35:691–5. doi:10.1016/S1872-5813(08)60004-3.

[49] Chellappa AS, Fischer CM, Thomson WJ. Ammonia decomposition kinetics over Ni-Pt/Al_2O_3 for PEM fuel cell applications. Appl Catal A Gen 2002;227:231–40. doi:10.1016/S0926-860X(01)00941-3.

[50] Liang C, Li W, Wei Z, Xin Q, Li C. Catalytic decomposition of ammonia over nitrided MoNx/α-Al_2O_3 and NiMoNy/α -Al_2O_3 catalysts. Ind Eng Chem Res 2000;39:3694–7. doi:10.1021/ie990931n.

[51] Leybo DV, Baiguzhina AN, Muratov DS, Arkhipov DI, Kolesnikov EA, Levina VV, et al. Effects of composition and production route on structure and catalytic activity for ammonia decomposition reaction of ternary Ni-Mo nitride catalysts. Int J Hydrogen Energy 2015;41:3854–60. doi:10.1016/j.ijhydene.2015.12.171.

[52] Polanski J, Bartczak P, Ambrozkiewicz W, Sitko R, Siudyga T, Mianowski A, et al. Ni-supported Pd nanoparticles with Ca promoter: A new catalyst for low-temperature ammonia cracking. PLoS One 2015;10(8). doi:10.1371/journal.pone.0136805.

[53] Simonsen SB, Chakraborty D, Chorkendorff I, Dahl S. Alloyed Ni-Fe nanoparticles as catalysts for NH_3 decomposition. Appl Catal A Gen 2012;447–448:22–31. doi:10.1016/j.apcata.2012.08.045.

[54] Trovarelli A, Llorca J. Ceria Catalysts at Nanoscale: How Do Crystal Shapes Shape Catalysis? ACS Catal 2017;7:4716–35. doi:10.1021/acscatal.7b01246.

[55] Melchionna M, Fornasiero P. The role of ceria-based nanostructured materials in energy applications. Mater Today 2014;17:349–57. doi:10.1016/j.mattod.2014.05.005.

[56] Muroyama H, Saburi C, Matsui T, Eguchi K. Ammonia decomposition over Ni/La_2O_3 catalyst for on-site generation of hydrogen. Appl Catal A Gen 2012;443–444:119–24. doi:10.1016/j.apcata.2012.07.031.

[57] Deng QF, Zhang H, Hou XX, Ren TZ, Yuan ZY. High-surface-area $Ce_{0.8}Zr_{0.2}O_2$ solid solutions supported Ni catalysts for ammonia decomposition to hydrogen. Int J Hydrogen Energy 2012;37:15901–7. doi:10.1016/j.ijhydene.2012.08.069.

[58] Liu H, Wang H, Shen J, Sun Y, Liu Z. Promotion effect of cerium and lanthanum oxides on Ni/SBA-15 catalyst for ammonia decomposition. Catal Today 2008;131:444–9. doi:10.1016/j.cattod.2007.10.048.

[59] Yao L, Shi T, Li Y, Zhao J, Ji W, Au C-T. Core–shell structured nickel and ruthenium nanoparticles: Very active and stable catalysts for the generation of COx-free hydrogen via ammonia decomposition. Catal Today 2011;164:112–8. doi:10.1016/j.cattod.2010.10.056.

[60] Zhao Z, Zou H, Lin W. Effect of rare earth and other cationic promoters on properties of CoMoNx/CNTs catalysts for ammonia decomposition. J Rare Earths 2013;31:247–50. doi:10.1016/S1002-0721(12)60266-X.

[61] Podila S, Alhamed YA, Alzahrani AA, Petrov LA. Hydrogen production by ammonia decomposition using Co catalyst supported on Mg mixed oxide systems. Int J Hydrogen Energy 2015;40:15411–22. doi:10.1016/j.ijhydene.2015.09.057.

[62] Divins NJ, Casanovas A, Xu W, Senanayake SD, Wiater D, Trovarelli A, et al. The influence of nano-architectured CeO_x supports in $RhPd/CeO_2$ for the catalytic ethanol steam reforming reaction. Catal Today 2015;253:99–105. doi:10.1016/j.cattod.2014.12.042.

[63] Mullins DR, Overbury SH, Huntley DR. Electron spectroscopy of single crystal and polycrystalline cerium oxide surface. Surf Sci 1998;409:307–19. doi:10.1016/S0039-6028(98)00257-X.

[64] Rotole JA, Sherwood PMA. Gamma-Alumina (γ-Al_2O_3) by XPS. Surf Sci Spectra 1998;5:18–24. doi:10.1116/1.1247852.

[65] Davidson A, Tempere JF, Che M, Roulet H, Dufour G. Spectroscopic studies of nickel(II) and nickel(III) species generated upon thermal treatments of nickel/ceria-supported materials. J Phys Chem 1996;100:4919–29. doi:10.1021/jp952268w.

[66] Roy B, Leclerc CA. Study of preparation method and oxidization/reduction effect on the performance of nickel-cerium oxide catalysts for aqueous-phase reforming of ethanol. J Power Sources 2015;299:114–24. doi:10.1016/j.jpowsour.2015.08.069.

[67] Mansour AN, Melendres CA. Characterization of $Ni_2O_3 \cdot 6H_2O$ by XPS. Surf Sci Spectra 1994;3:263–70. doi:10.1116/1.1247755.

[68] Biesinger MC, Payne BP, Lau LWM, Gerson A, Smart RSC. X-ray photoelectron spectroscopic chemical state quantification of mixed nickel metal, oxide and hydroxide systems. Surf Interface Anal 2009;41:324–32. doi:10.1002/sia.3026.

[69] Morgan DJ. Resolving ruthenium: XPS studies of common ruthenium materials. Surf Interface Anal 2015;47:1072–9. doi:10.1002/sia.5852.

[70] Bianchi CL, Ragaini V, Cattania MG. An XPS study on ruthenium compounds and catalysts. Mater Chem Phys, 1991;29:297-306.doi:10.1016/0254-0584(91)90025-P.

[71] Elmasides C, Kondarides DI, Grünert W, Verykios XE. XPS and FTIR Study of Ru/Al_2O_3 and Ru/TiO_2 Catalysts: Reduction Characteristics and Interaction with a Methane−Oxygen Mixture. J Phys Chem B 1999;103:5227–39. doi:10.1021/jp9842291.

[72] Yin SF, Zhang QH, Xu BQ, Zhu WX, Ng CF, Au CT. Investigation on the catalysis of CO_x-free hydrogen generation from ammonia. J Catal 2004;224:384–96.

doi:10.1016/j.jcat.2004.03.008.

[73] Wang SJ, Yin SF, Li L, Xu BQ, Ng CF, Au CT. Investigation on modification of Ru/CNTs catalyst for the generation of CO_x-free hydrogen from ammonia. Appl Catal B Environ 2004;52:287–99. doi:10.1016/j.apcatb.2004.05.002.

[74] Yin SF, Xu BQ, Zhu WX, Ng CF, Zhou XP, Au CT. Carbon nanotubes-supported Ru catalyst for the generation of CO_x-free hydrogen from ammonia. Catal Today 2004;93–95:27–38. doi:10.1016/j.cattod.2004.05.011.

[75] Choudhary TV, Sivadinarayana C, Goodman DW. Catalytic ammonia decomposition: CO_x-free hydrogen production for fuel cell applications. Catal Letters 2001;72:197–201. doi:10.1023/A:1009023825549.

[76] Yao HC, Yao YFY. Ceria in automotive exhaust catalysts. I. Oxygen storage. J Catal 1984;86:254–65. doi:10.1016/0021-9517(84)90371-3.

[77] Gnanamani MK, Ribeiro MC, Ma W, Shafer WD, Jacobs G, Graham UM, et al. Fischer-Tropsch synthesis: Metal-support interfacial contact governs oxygenates selectivity over CeO_2 supported Pt-Co catalysts. Appl Catal A Gen 2011;393:17–23. doi:10.1016/j.apcata.2010.11.019.

[78] Laachir A, Perrichon V, Badri A, Lamotte J, Catherine E, Lavalley JC, et al. Reduction of CeO_2 by Hydrogen. J Chem Soc Faraday Trans,1991;87:1601–9. doi:10.1039/FT9918701601.

[79] Jacobs G, Patterson PM, Williams L, Sparks D, Davis BH. Low temperature water-gas shift: role of pretreatment on formation of surface carbonates and formates. Catal Letters 2004;96:97–105. doi:10.1023/B:CATL.0000029536.52909.92.

[80] Jacobs G, Graham UM, Chenu E, Patterson PM, Dozier A, Davis BH. Low-

temperature water-gas shift: impact of Pt promoter loading on the partial reduction of ceria and consequences for catalyst design. J Catal 2005;229:499–512. doi:10.1016/j.jcat.2004.11.031.

[81] Sharma V, Crozier PA, Sharma R, Adams JB. Direct observation of hydrogen spillover in Ni-loaded Pr-doped ceria. Catal Today 2012;180:2–8. doi:10.1016/j.cattod.2011.09.009.

[82] Wang J, Shen M, Wang J, Yang M, Wang W, Ma J, et al. Effects of Ni-doping of ceria-based materials on their micro-structures and dynamic oxygen storage and release behaviors. Catal Letters 2010;140:38–48. doi:10.1007/s10562-010-0420-2.

[83] Aouad S, Saab E, Abi Aad E, Aboukaïs A. Reactivity of Ru-based catalysts in the oxidation of propene and carbon black. Catal Today 2007;119:273–7. doi:10.1016/j.cattod.2006.08.030.

[84] Wang M, Au CT, Lai SY. H_2 production from catalytic steam reforming of n-propanol over ruthenium and ruthenium-nickel bimetallic catalysts supported on ceria-alumina oxides with different ceria loadings. Int J Hydrogen Energy 2015;40:13926–35. doi:10.1016/j.ijhydene.2015.07.162.

[85] Wefers K, Misra C. Oxides and Hydroxides of Aluminum. Alcoa Tech Pap 1987;19:1–100.

[86] Miletić N, Izquierdo U, Obregón I, Bizkarra K, Agirrezabal-Telleria I, Bario LV., et al. Oxidative steam reforming of methane over nickel catalysts supported on Al_2O_3–CeO_2–La_2O_3. Catal Sci Technol 2015;5:1704–15. doi:10.1039/C4CY01438C.

[87] He CZ, Wang H, Huai LY, Liu JY. Mechanism of ammonia decomposition and oxidation on Ir(100): A first-principles study. J Phys Chem C 2012;116:24035–45. doi:10.1021/jp305399g.